

# Construction of BiVO<sub>4</sub>@NiCo<sub>2</sub>O<sub>3</sub> Heterojunction to Promote Photocatalytic CO<sub>2</sub> Reduction

Wenjie Fu,<sup>[a]</sup> Guanhong Lu,<sup>[b]</sup> Xiao Wang,<sup>[b]</sup> Xiaofeng Xie,<sup>[b]</sup> and Jing Sun<sup>\*[b]</sup>

Constructing a catalyst capable of reducing CO<sub>2</sub> through photoreduction in aqueous environments presents a significant challenge. In this study, we present the synthesis of BiVO<sub>4</sub>@NiCo<sub>2</sub>O<sub>3</sub> heterojunction using a straightforward hydrothermal method for CO<sub>2</sub> photoreduction. The sample with the optimal loading ratio demonstrates a CO generation rate of 7.202 μmol·g<sup>-1</sup>·h<sup>-1</sup>, which is twice that of pure BiVO<sub>4</sub>

(3.626 μmol·g<sup>-1</sup>·h<sup>-1</sup>) and 1.5 times that of pure NiCo<sub>2</sub>O<sub>3</sub> (4.726 μmol·g<sup>-1</sup>·h<sup>-1</sup>). Analysis using XPS and EPR techniques suggests that electron transfer at the interface of the heterojunction facilitates the separation of photogenerated charge carriers, thereby enhancing the efficiency of the photocatalytic process. This investigation offers a viable approach for developing photocatalysts for CO<sub>2</sub> reduction in aqueous environments.

## Introduction

The extensive exploitation and utilization of fossil fuels has resulted in a significant rise in anthropogenic carbon dioxide emissions. As a result, a multitude of environmental issues, including the greenhouse effect, are increasingly worsening. In this context, utilizing solar energy for carbon dioxide photoreduction (CO<sub>2</sub>PR) is considered as a promising and prospective solution to tackle the issues.<sup>[1]</sup> Photocatalytic CO<sub>2</sub> reduction in aqueous environments involves two half-reactions: photoinduced hole-driven water oxidation and electron-proton-induced reduction of CO<sub>2</sub>. This requires that the conduction band potential of the catalyst be more negative than the reduction potential of CO<sub>2</sub>, for example the reduction potential of CO<sub>2</sub>/CO (-0.53 V vs. NHE, pH=7). The valence band must surpass the oxidation potential of oxygen molecules, such as the oxidation potential of O<sub>2</sub>/H<sub>2</sub>O (+0.82 V vs. NHE, pH=7).<sup>[2]</sup> Therefore, achieving complete CO<sub>2</sub> conversion with a single semiconductor material poses a significant challenge.

Various techniques, including ion doping,<sup>[3]</sup> formation of solid solution,<sup>[4]</sup> heterojunction construction,<sup>[5]</sup> and defect introduction,<sup>[6]</sup> have been used to accomplish both efficient light absorption and sufficient reduction capability. The construction of heterojunctions is advantageous for optimizing the light absorption range, enhancing selectivity and reduction efficiency, and increasing stability, thus being regarded as an effective approach for resolving this issue.<sup>[7]</sup> Tahir et al.<sup>[8]</sup> synthesized a g-C<sub>3</sub>N<sub>4</sub>/TiO<sub>2</sub>/Ti<sub>3</sub>AlC<sub>2</sub> composite with a 2D/0D/2D heterostructure by simple heat treatment and calcination. It

was found that TiO<sub>2</sub> nanoparticles exhibit faster carrier separation rates and higher CH<sub>4</sub> production rates when combined with Ti<sub>3</sub>AlC<sub>2</sub> compared to larger TiO<sub>2</sub> microparticles (MPs). Under visible light irradiation, ternary composites using Ti<sub>3</sub>AlC<sub>2</sub>-anchored TiO<sub>2</sub> nanoparticles combined with g-C<sub>3</sub>N<sub>4</sub> achieved a CH<sub>4</sub> yield of up to 2103.5 μmol·g<sup>-1</sup>·h<sup>-1</sup> and a selectivity of 96.59%. Zhang et al.<sup>[9]</sup> used a hydrothermal method to obtain a 0D/1D Ag<sub>2</sub>S/Sb<sub>2</sub>S<sub>3</sub> heterojunction by synthesizing Ag<sub>2</sub>S quantum dots in-situ on Sb<sub>2</sub>S<sub>3</sub> nanorods. The methane generation rate of the sample was 6.75 μmol·g<sup>-1</sup>·h<sup>-1</sup>, with a selectivity of 96.1%. In-situ Fourier transform infrared spectroscopy and Gibbs free energy calculations revealed that the Ag–Sb bimetallic composite provides sites for forming stable Ag–C–O–Sb configurations, which is critical for the conversion of CO<sub>2</sub> to CH<sub>4</sub>. Li et al.<sup>[10]</sup> successfully prepared Au clusters/TiO<sub>2</sub>/Ti<sub>3</sub>C<sub>2</sub> and Au nanoparticle/TiO<sub>2</sub>/Ti<sub>3</sub>C<sub>2</sub> using the deposition-precipitation method. The research results demonstrate that Au clusters/TiO<sub>2</sub>/Ti<sub>3</sub>C<sub>2</sub> with quantum size effect exhibit higher photocatalytic CO<sub>2</sub> reduction activity compared to Au nanoparticle/TiO<sub>2</sub>/Ti<sub>3</sub>C<sub>2</sub> with surface plasmon resonance. The yields of CO and CH<sub>4</sub> are 9.17 μmol·g<sup>-1</sup>·h<sup>-1</sup> and 14.04 μmol·g<sup>-1</sup>·h<sup>-1</sup>, respectively. The overlapping orbitals formed between the lowest unoccupied molecular orbital of Au nanoclusters and the antibonding orbital of CO<sub>2</sub> effectively enhance the activation efficiency of CO<sub>2</sub>.

Cobalt oxides are considered as reasonable CO<sub>2</sub>PR catalysts due to the abundance of cobalt sites on surface for CO<sub>2</sub> adsorption and activation.<sup>[11]</sup> Among them, Rock-salt oxides such as nickel cobaltite (Ni<sub>x</sub>Co<sub>y</sub>O<sub>x+y</sub>) have been widely utilized in photocatalysis and electrochemistry due to their high carrier density and redox activity. However, there is only few research on their application in CO<sub>2</sub>PR.<sup>[12]</sup> Li et al.<sup>[13]</sup> developed a multi-step templating method to construct double-shelled nanoboxes using Cu<sub>2</sub>S and hydroxy-rich NiCo<sub>2</sub>O<sub>3</sub>. The abundant active sites and rapid charge transfer and separation significantly promoted the ability to reduce CO<sub>2</sub> to CO, and the surface hydroxyl content plays a crucial role in regulating the activity and selectivity of CO<sub>2</sub> reduction. Still, the limited absorption of visible light by nickel cobaltite, coupled with its

[a] W. Fu  
College of Chemistry and Materials Science  
Shanghai Normal University  
Shanghai 200234 (P. R. China)

[b] G. Lu, Dr. X. Wang, Prof. X. Xie, Prof. J. Sun  
State Key Lab of High Performance Ceramics and Superfine Microstructure  
Shanghai Institute of Ceramics  
Chinese Academy of Sciences  
Shanghai 201899 (P. R. China)  
E-mail: jingsun@mail.sic.ac.cn

rapid photogenerated carrier recombination, constrains its application in CO<sub>2</sub>PR.

Most bismuth-based semiconductor materials have band gaps below 3.0 eV, demonstrating excellent visible light absorption properties.<sup>[14]</sup> Among them, bismuth vanadate (BiVO<sub>4</sub>) stands out with a narrower band gap of 2.4–2.5 eV, an environmentally friendly nature, and chemical stability. The monoclinic phase of BiVO<sub>4</sub> exhibits good performance for water oxidation, releasing oxygen and active substances, making it a promising oxidative photocatalyst.<sup>[15,16]</sup> Philo et al.<sup>[17]</sup> used template-directed strategies to prepare ultra-thin 2D monoclinic BiVO<sub>4</sub> nanosheets that exhibited excellent photocatalytic OER performance. The quantum efficiency is up to 69.4%, due to the modulation of charge carriers dynamics and catalytic surface features. Zhang et al.<sup>[17]</sup> prepared a photoanode for photoelectrochemical water splitting by modifying surface-chlorinated BiVO<sub>4</sub> with a nickel hydroxide co-catalyst. The appropriate electronegative Cl<sup>-</sup> modification significantly enhanced the photoelectrochemical water oxidation activity of BiVO<sub>4</sub>. The composite photoanode achieved a photocurrent density of 4.33 mA·cm<sup>-2</sup> at 1.23 V vs. RHE, which is approximately three times higher than that of pure BiVO<sub>4</sub>. Moreover, significant improvements were observed in the apparent photon-to-current conversion efficiency (ABPE), incident photon-to-charge carrier efficiency (IPCE), and charge separation efficiency.

Despite significant progress in the research of CO<sub>2</sub> photocatalysts for several decades, using pure water without any sacrificial agents as an electron and proton donor for CO<sub>2</sub>PR remains challenging. In this study, NiCo<sub>2</sub>O<sub>3</sub> was synthesized in-situ on the surface of BiVO<sub>4</sub> to construct a BiVO<sub>4</sub>@NiCo<sub>2</sub>O<sub>3</sub> heterojunction catalyst. On the one hand, BiVO<sub>4</sub> can provide electrons to NiCo<sub>2</sub>O<sub>3</sub> and promote the reduction of CO<sub>2</sub>. On the other hand, the heterojunction construction facilitates the efficient migration and separation of photogenerated electron-hole pairs in NiCo<sub>2</sub>O<sub>3</sub>, thereby enhancing its photocatalytic efficiency. Various proportions of NiCo<sub>2</sub>O<sub>3</sub> in the composites were adjusted to examine their impact on the photocatalytic performance of CO<sub>2</sub> reduction. The experimental results indicate that the CO<sub>2</sub> photoreduction performance of the BiVO<sub>4</sub>@NiCo<sub>2</sub>O<sub>3</sub> sample at the optimal loading ratio is significantly enhanced, achieving 1.5 times that of the pure NiCo<sub>2</sub>O<sub>3</sub> sample with a CO production rate of 7.202 μmol·g<sup>-1</sup>·h<sup>-1</sup>.

## Experiment Section

### Material Preparation

Bismuth chloride (BiCl<sub>3</sub>), sodium metavanadate (NaVO<sub>3</sub>), cetyltrimethylammonium bromide (CTAB), nickel nitrate hexahydrate (Ni(NO<sub>3</sub>)<sub>2</sub>·6H<sub>2</sub>O), cobalt nitrate hexahydrate (Co(NO<sub>3</sub>)<sub>2</sub>·6H<sub>2</sub>O), trisodium citrate, hexamethylenetetramine, and polyvinylpyrrolidone (PVP, K30) were purchased from Shanghai Adamas Reagent Co., Ltd. Anhydrous ethanol was produced by Sinopharm Chemical Reagent Co., Ltd. All chemical reagents were of analytical grade and used without further purification. Deionized water prepared from an ultrapure water system (Tondino Scientific (Shanghai) Co., Ltd.) was used throughout the entire experimental process.

### Synthesis of BiVO<sub>4</sub> and BiVO<sub>4</sub>@NiCo<sub>2</sub>O<sub>3</sub> Heterojunction

BiVO<sub>4</sub> was synthesized following the established synthesis methods reported in the literature.<sup>[15b]</sup> A solution of BiCl<sub>3</sub> (2.21 g) and cetyltrimethylammonium bromide (CTAB, 1.05 g) in ethylene glycol (60 mL) was prepared. NaVO<sub>3</sub> (2.80 g) was added to the solution, and the mixture was stirred for 30 min. Subsequently, the solution was transferred to a 100 mL high-pressure autoclave lined with polytetrafluoroethylene and reacted at 120 °C for 12 h. After the reactor cooled to room temperature, the product was washed with ethanol and deionized water multiple times to get a yellow-green solid. The solid was then dried in a vacuum oven at 60 °C for 12 h, followed by calcination at 450 °C for 8 min, yielding the final BiVO<sub>4</sub> product.

The synthesis of the BiVO<sub>4</sub>@NiCo<sub>2</sub>O<sub>3</sub> heterojunction was performed following the established methods described in the literature.<sup>[13]</sup> BiVO<sub>4</sub>@NiCo<sub>2</sub>O<sub>3-x</sub> (x = 0.67, 1, 2, 5, representing the molar ratio of Ni(NO<sub>3</sub>)<sub>2</sub>·6H<sub>2</sub>O to BiVO<sub>4</sub>) was prepared by hydrothermal and annealing steps. BiVO<sub>4</sub> (0.5 g), ethanol (20 mL), and deionized water (100 mL) were mixed using ultrasonic treatment for 30 min. Under magnetic stirring, Ni(NO<sub>3</sub>)<sub>2</sub>·6H<sub>2</sub>O (0.299 g), Co(NO<sub>3</sub>)<sub>2</sub>·6H<sub>2</sub>O (0.599 g), and PVP surfactant (0.4 g) were added to the suspension, followed by adding trisodium citrate (0.319 g) and hexamethylenetetramine (1.731 g). After 10 minutes of stirring, the reaction mixture was refluxed in a water bath at 90 °C with stirring for 6 hours. Then, it was cooled to room temperature. The solid product was subjected to centrifugal washing using deionized water and ethanol, followed by vacuum drying at 60 °C. This process was repeated for three cycles. The product was annealed for 2 hours at 300 °C in a nitrogen environment at a heating rate of 2 °C·min<sup>-1</sup>, generating the product denoted as BiVO<sub>4</sub>@NiCo<sub>2</sub>O<sub>3-0.67</sub>. Identical procedures were followed for other BiVO<sub>4</sub>@NiCo<sub>2</sub>O<sub>3-x</sub> but changing metal nitrate weights. The amounts of Ni(NO<sub>3</sub>)<sub>2</sub>·6H<sub>2</sub>O and Co(NO<sub>3</sub>)<sub>2</sub>·6H<sub>2</sub>O were 0.449 g and 0.899 g for x = 1, 0.897 g and 1.797 g for x = 2, and 2.243 g and 4.493 g for x = 5, respectively. Pure NiCo<sub>2</sub>O<sub>3</sub> samples were prepared as a control without the addition of BiVO<sub>4</sub>.

### Characterization

The phase composition of the samples was characterized using powder X-ray diffraction (PXRD) with a Bruker D8 ADVANCE diffractometer equipped with Cu-Kα radiation. The scanning range was set to 2θ angles of 10–80°, and the scanning rate was 2°/min. The specific surface area and pore distribution of the samples were investigated using nitrogen adsorption-desorption measurements conducted on a Micromeritics 3Flex automatic surface area and porosity analyzer. X-ray photoelectron spectroscopy (XPS) analysis of the samples was performed (ESCALAB250, USA) to study the oxidation states and surface chemical environments of various elements. The morphology and microstructure of the samples were examined using field-emission scanning electron microscopy (Verios G4, USA) and transmission electron microscopy (JEM-2100F, Japan). The optical absorption behavior of different samples was studied using ultraviolet-visible diffuse reflectance spectroscopy (DRS) with a Cary 5000 instrument. Photoluminescence spectroscopy measurements were carried out on a Perkin Elmer instrument (USA) to obtain the information on electrons and holes of the samples with the excitation wavelength at 300 nm. Transient photocurrent measurements, electrochemical impedance spectroscopy, and Mott-Schottky analysis of the samples were conducted using a photoelectrochemical workstation (CH Instrument Company, Shanghai) equipped with a three-electrode system. The capture of active free radicals was investigated using an electron spin resonance spectrometer (ESR) with a Bruker EMXplus-6/1 instrument. Gas chromatography (Agilent 7890B GC) combined with a flame ionization detector (FID) was employed to detect the

concentrations of CO and CH<sub>4</sub> during the photocatalytic process. Photoluminescence spectroscopy measurements were carried out on a Perkin Elmer instrument (USA) to obtain the information on electrons and holes of the samples with the excitation wavelength at 300 nm. In-situ XPS (ThermoFisher ESCALAB 250Xi) is used to detect changes in electron cloud density under irradiation. Fluorescence spectrum measurements were carried out on an Edinburgh FLS1000 (UK) to detect formed hydroxyl radical amounts.

### Photocatalytic Performance

A closed photocatalytic reactor with a volume of 440 ml was employed to conduct photocatalytic performance. The reactor was loaded with 10 mg of catalyst and 10 ml of deionized water, and high-purity CO<sub>2</sub> gas was introduced for 30 min. After that, the inlet and outlet of the reactor were sealed. A 420 W xenon lamp served as the light source for the photocatalytic reduction of CO<sub>2</sub>. Throughout the reaction, the temperature was maintained at 20 °C by circulating cooling water. Gas samples are extracted from the reactor using a sampling needle. Gas chromatography is employed for the analysis of CO<sub>2</sub> reduction products, while hydrogen gas sensors are utilized to detect potential hydrogen generation during the reaction.

## Results and Discussion

Scanning electron microscopy (SEM) images in Figure 1 illustrate the morphology of the bare BiVO<sub>4</sub> and samples with varying ratios of NiCo<sub>2</sub>O<sub>3</sub> encapsulation. A comparison between the images of BiVO<sub>4</sub> and BiVO<sub>4</sub>@NiCo<sub>2</sub>O<sub>3</sub>-0.67 samples reveals partial growth of synthesized NiCo<sub>2</sub>O<sub>3</sub> on the BiVO<sub>4</sub> surface, accompanied by agglomeration of amorphous particles. In the images of the BiVO<sub>4</sub>@NiCo<sub>2</sub>O<sub>3</sub>-2 and BiVO<sub>4</sub>@NiCo<sub>2</sub>O<sub>3</sub>-5 samples,

the exposed surface of BiVO<sub>4</sub> is barely observable. Energy-dispersive X-ray (EDX) elemental mapping in Figure 2 demonstrates the distribution of Bi, V, O, Ni, and Co on the surface of the BiVO<sub>4</sub>@NiCo<sub>2</sub>O<sub>3</sub>-2 sample, confirming the successful coating of NiCo<sub>2</sub>O<sub>3</sub> onto BiVO<sub>4</sub>.

Powder X-ray diffraction (XRD) patterns validated the successful synthesis of NiCo<sub>2</sub>O<sub>3</sub> and BiVO<sub>4</sub>. As depicted in Figure 3, the NiCo<sub>2</sub>O<sub>3</sub> exhibits a broad peak width. Interestingly, CoO and NiO have almost identical XRD patterns and lattice parameters (0.067 Å deviation).<sup>[12c]</sup> Some Ni atoms could be substituted into CoO lattices, where Ni and Co atoms occupy octahedral interstices.<sup>[19]</sup> No split peaks or shoulders are observed, indicating the formation of single-phase NiCo<sub>2</sub>O<sub>3</sub> rather than mixtures. Synthesized BiVO<sub>4</sub> shows high crystallinity and can be indexed to the monoclinic phase (JCPDS no. 14-0688). The XRD pattern of the prepared BiVO<sub>4</sub>@NiCo<sub>2</sub>O<sub>3</sub>-2 sample is similar to BiVO<sub>4</sub> and has a low peak intensity of NiCo<sub>2</sub>O<sub>3</sub>. This could be attributed to the poor crystallinity of NiCo<sub>2</sub>O<sub>3</sub>.

Figure 4 shows the transmission electron microscopy (TEM) images. The TEM image of BiVO<sub>4</sub> displays a thin, wrinkled or stacked, and irregular block structure. High-resolution TEM (HRTEM) of the BiVO<sub>4</sub>@NiCo<sub>2</sub>O<sub>3</sub>-2 sample reveals lattice fringes perpendicular to different planes, with lattice plane spacings of 0.21 and 0.28 nm corresponding to the (2,0,0) and (0,4,0) planes of NiO and BiVO<sub>4</sub>, respectively. These results suggest the formation of a close heterostructure between NiCo<sub>2</sub>O<sub>3</sub> and BiVO<sub>4</sub>.

X-ray photoelectron spectroscopy (XPS) revealed changes in the chemical composition and valence states. The Co 2p and Ni 2p spectra indicated the presence of both Co<sup>2+</sup> (780.9 and 796.4 eV) and Co<sup>3+</sup> (779.6 and 794.8 eV), Ni<sup>2+</sup> (854.0 and

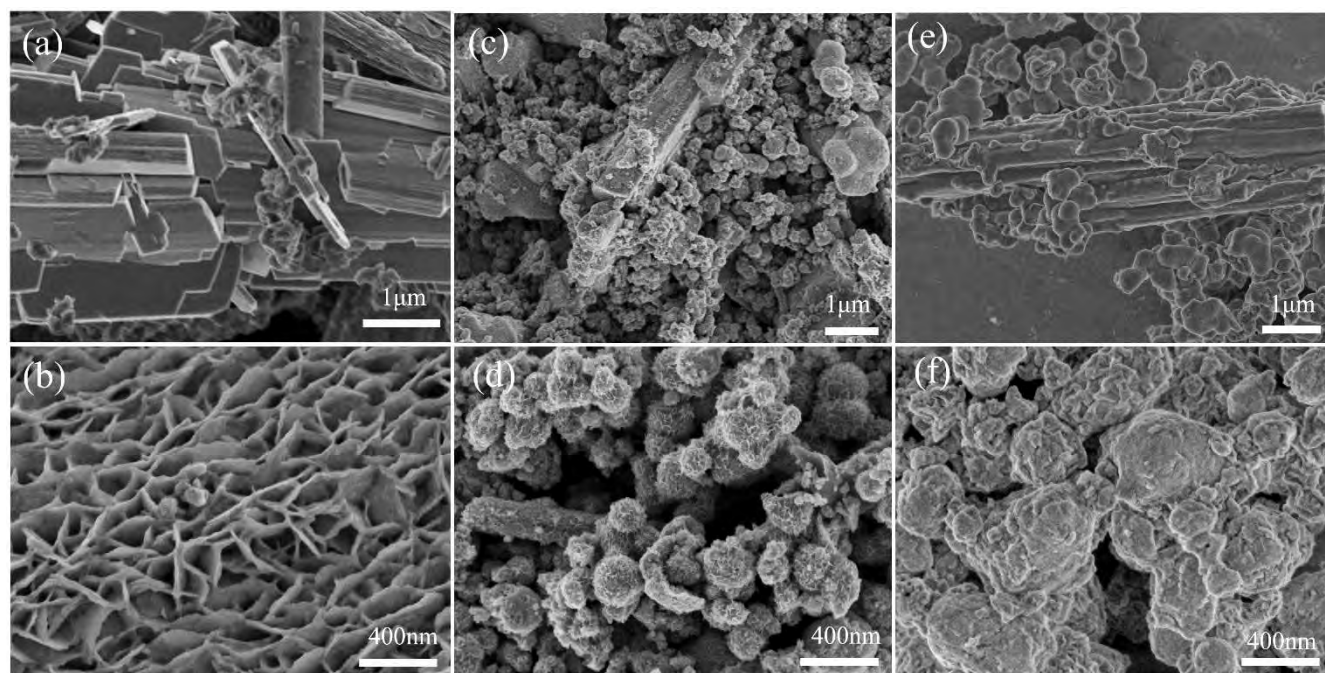


Figure 1. SEM images of (a, b) BiVO<sub>4</sub>, (c, d) BiVO<sub>4</sub>@NiCo<sub>2</sub>O<sub>3</sub>-0.67, (e) BiVO<sub>4</sub>@NiCo<sub>2</sub>O<sub>3</sub>-2, and (f) BiVO<sub>4</sub>@NiCo<sub>2</sub>O<sub>3</sub>-5.

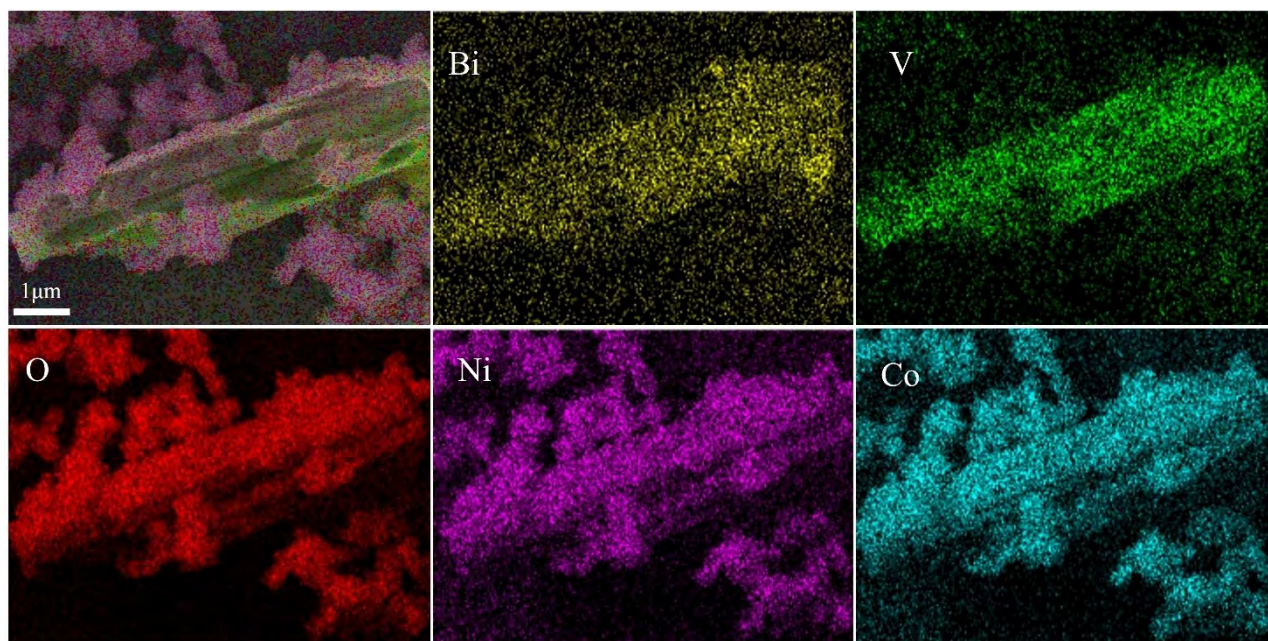


Figure 2. EDX elemental mapping pattern of the  $\text{BiVO}_4/\text{NiCo}_2\text{O}_3\text{-2}$  sample.

872.1 eV) and  $\text{Ni}^{3+}$  (855.5 and 873.5 eV), respectively.<sup>[12c,19]</sup> The characteristic peaks of Bi 4f and V 2p in the  $\text{BiVO}_4/\text{NiCo}_2\text{O}_3\text{-2}$  heterojunction were shifted toward higher binding energies (BEs), indicating an decrease in electron cloud density (Figure 5a, b). The characteristic peaks of Ni 2p and Co 2p in the  $\text{BiVO}_4/\text{NiCo}_2\text{O}_3\text{-2}$  heterojunction were shifted toward lower BEs than those of  $\text{NiCo}_2\text{O}_3$  (Figure 5c, d), indicating an increase in electron cloud density. These shifts suggest an electron transfer from Bi and V to Co and Ni in the system.

UV-Vis absorption spectroscopy was utilized to characterize the optical absorption properties of the samples. As depicted in Figure 6a, the composite heterojunction sample exhibits enhanced light absorption in the ultraviolet area compared to  $\text{BiVO}_4$ . In the visible region, the absorption performance of heterojunction samples is slightly lower than that of  $\text{BiVO}_4$  and

$\text{NiCo}_2\text{O}_3$ , and slightly higher than that of original  $\text{NiCo}_2\text{O}_3$  in the infrared area. The Tauc plot was employed to determine the band gaps of  $\text{BiVO}_4$  and  $\text{NiCo}_2\text{O}_3$ , resulting in values of 2.29 eV and 3.0 eV, respectively. The photocurrent measurements are presented in Figure 6d, indicating that the  $\text{BiVO}_4/\text{NiCo}_2\text{O}_3\text{-2}$  sample displayed the highest photocurrent response among the different compositions, implying its excellent charge separation performance under illumination. Based on Figure 6e, it is inferred that  $\text{BiVO}_4$  is an n-type semiconductor with a flat band potential of  $-0.5$  eV vs. Ag/AgCl. By calculation, the conduction band potential of  $\text{BiVO}_4$  relative to the reversible hydrogen electrode (RHE) is  $-0.09$  eV. Using the optical bandgap value obtained from Figure 6b, the valence band potential of  $\text{BiVO}_4$  is determined to be 2.2 eV vs. RHE. Similarly, for the synthesized  $\text{NiCo}_2\text{O}_3$ , its conduction and valence band potentials are calculated to be  $-1.61$  eV and 1.39 eV vs. RHE, respectively.

We evaluated the photocatalytic performance of  $\text{BiVO}_4/\text{NiCo}_2\text{O}_3\text{-x}$  heterojunction for  $\text{CO}_2$  conversion upon visible light irradiation. In the reaction, no sacrificial agents are added. Gas chromatography and liquid chromatography were employed to analyze potential products, which include  $\text{CO}$ ,  $\text{CH}_4$ , methanol, ethanol, and formic acid. The experimental results demonstrate that the reaction products are  $\text{CO}$  and  $\text{CH}_4$ , with no hydrogen or other reduction byproducts detected. Figure 7a shows that the  $\text{CO}_2$  reduction activity of the sample significantly increases compared with  $\text{BiVO}_4$  or pure  $\text{NiCo}_2\text{O}_3$ . Among them,  $\text{BiVO}_4/\text{NiCo}_2\text{O}_3\text{-2}$  exhibits the highest  $\text{CO}$  production rate, reaching up to  $7.202 \mu\text{mol}\cdot\text{g}^{-1}\cdot\text{h}^{-1}$ . After 5 cycles of reaction, there was no significant decrease observed in the photocatalytic performance of  $\text{BiVO}_4/\text{NiCo}_2\text{O}_3\text{-2}$  (Figure 7b). Moreover, the XRD patterns of the samples before and after the reaction (Figure 7c) remained essentially unchanged. These

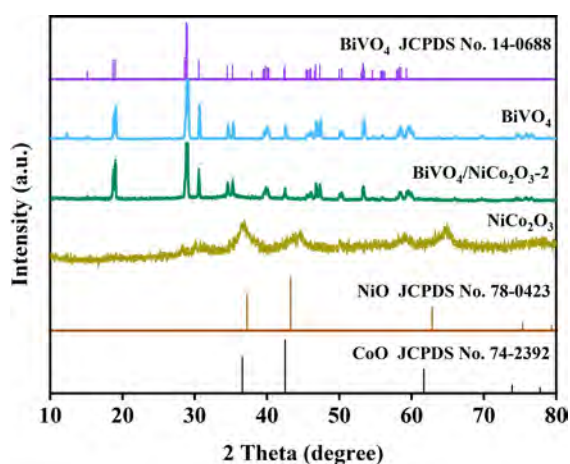
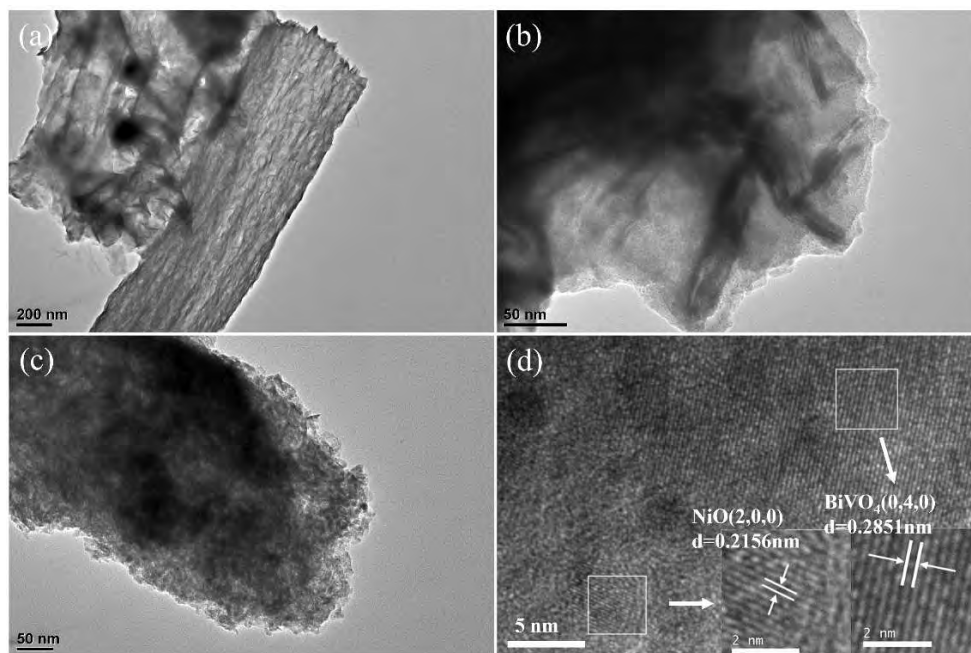
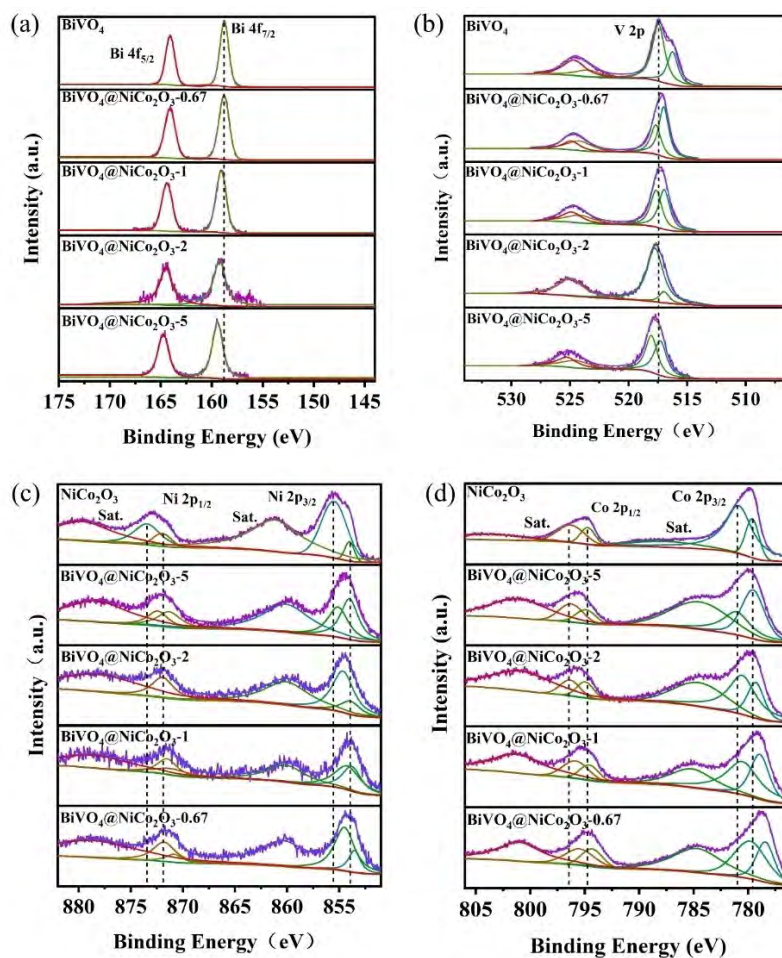


Figure 3. XRD patterns of the as-prepared different samples.



**Figure 4.** TEM images of (a)  $\text{BiVO}_4$ , (b)  $\text{BiVO}_4@ \text{NiCo}_2\text{O}_3-2$  and (c)  $\text{NiCo}_2\text{O}_3$  samples. (d) High-resolution transmission electron microscope image of  $\text{BiVO}_4@ \text{NiCo}_2\text{O}_3-2$ .



**Figure 5.** XPS spectra of (a) Bi 4f, (b) V 2p, (c) Ni 2p and (d) Co 2p of the prepared samples.

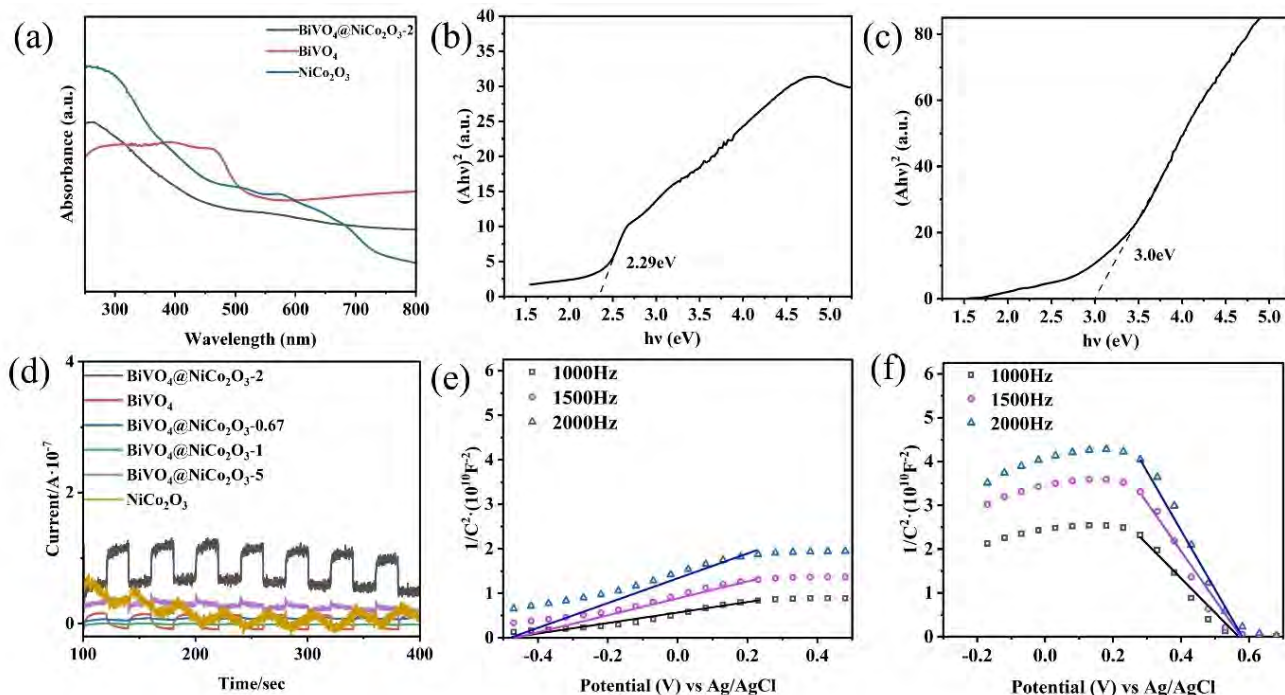


**Figure 6.** (a) UV-Vis absorption spectra of  $\text{BiVO}_4$ ,  $\text{BiVO}_4@/\text{NiCo}_2\text{O}_3-2$ , and  $\text{NiCo}_2\text{O}_3$  samples. Tauc plots of (b)  $\text{BiVO}_4$  and (c)  $\text{NiCo}_2\text{O}_3$  were obtained from the UV-Vis absorption spectra. (d) Photocurrent response tests of the prepared samples. (e, f) Mott-Schottky curves of  $\text{BiVO}_4$  and  $\text{NiCo}_2\text{O}_3$  at different frequencies.

results indicate the stability of the prepared photocatalyst. We conducted control experiments under identical conditions without a light source, in which no reduction products were detected in the dark, verifying that the process was light-driven. We also conducted additional control experiments under  $\text{N}_2$  atmosphere with the same conditions, in which no carbon products were observed, confirming  $\text{CO}_2$  gas as the only carbon source for reduction products. Compared to certain previously reported single-component semiconductor catalysts in Table 1, heterogeneous catalysts demonstrate significant potential for improving the performance of  $\text{CO}_2$  reduction in pure water environments. In addition, by selecting suitable materials for constructing heterogeneous junctions, it is possible to avoid

the utilization of precious metals or biotoxin metals, thereby aligning with the principles of green chemistry.

In-situ XPS was used to further confirm the electron transfer process occurring on the surface of  $\text{BiVO}_4$  and  $\text{NiCo}_2\text{O}_3$ . The binding energy of Bi 4f peaks shifted positively by 0.13 eV under light irradiation compared to the dark condition (Figure 8a). Similarly, in Figure 8b, the binding energy of V 2p peaks was also shifted positively by 0.51 eV under light-on conditions. Meanwhile, the binding energy of Co 2p peaks shifted negatively by 0.15 eV under visible-light irradiation (Figure 8d). This finding demonstrates a surface charge transfer process between  $\text{BiVO}_4$  and  $\text{NiCo}_2\text{O}_3$  under in-situ light-on conditions

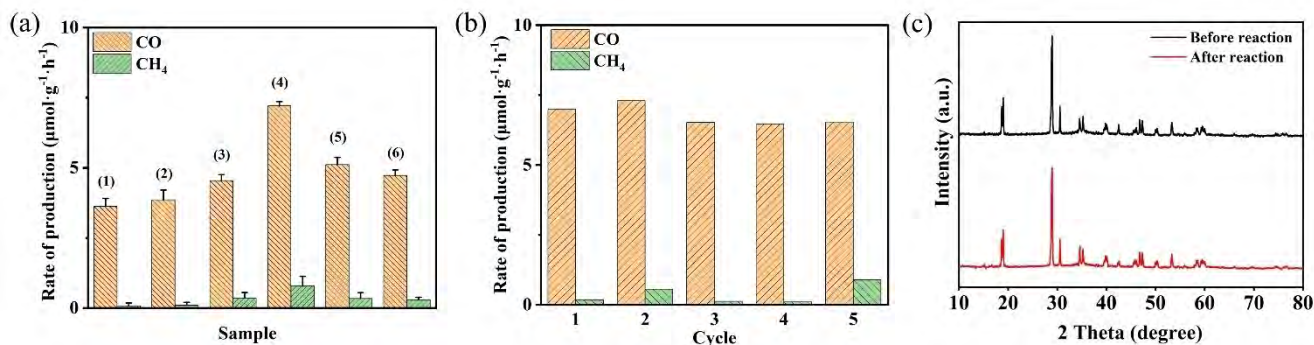


**Figure 7.** (a) Photocatalytic properties of (1)  $\text{BiVO}_4$ , (2)  $\text{BiVO}_4@/\text{NiCo}_2\text{O}_3-0.67$ , (3)  $\text{BiVO}_4@/\text{NiCo}_2\text{O}_3-1$ , (4)  $\text{BiVO}_4@/\text{NiCo}_2\text{O}_3-2$ , (5)  $\text{BiVO}_4@/\text{NiCo}_2\text{O}_3-5$  and (6)  $\text{NiCo}_2\text{O}_3$ , each sample was tested for three times to get error bar. (b) Photocatalytic cycle test for  $\text{BiVO}_4@/\text{NiCo}_2\text{O}_3-2$ . (c) XRD patterns of  $\text{BiVO}_4@/\text{NiCo}_2\text{O}_3-2$  sample before and after photocatalysis.

Catalyst	Reaction medium	Light source	Products	Activity ( $\mu\text{mol}\cdot\text{g}^{-1}\cdot\text{h}^{-1}$ )	References
$\text{BiVO}_4@/\text{NiCo}_2\text{O}_3-2$	Liquid-solid, water	420 W Xe Lamp	$\text{CO}$ $\text{CH}_4$	7.202 0.778	This work
2D Zn-MOF/BVON	Liquid-solid, water	Visible Light	$\text{CO}$ $\text{CH}_4$	4.31 0.62	[15b]
Co-MOF/ $\text{Cu}_2\text{O}$	Liquid-solid, water	Visible Light	$\text{CO}$	3.83	[21]
$\text{BiOBr}$	Liquid-solid, water	Xe Lamp	$\text{CO}$ $\text{CH}_4$	21.6 1.2	[22]
$\text{BiVO}_4\text{-Bi}_2\text{O}_3$	Gas-solid, water	Visible Light	$\text{CO}$ $\text{CH}_4$	0.42 3.29	[23]
$\text{BiVO}_4/\text{carbon-coated Cu}_2\text{O}$	Gas-solid, water	Visible Light	$\text{CO}$	3.01	[24]
$\text{NH}_2\text{-MIL-125(Ti)}$	Liquid-solid, $\text{H}_2\text{O}/\text{MeCN}/\text{TEOA}$	300 W Xe Lamp (AM 1.5 G)	$\text{CO}$	8.25	[25]

during the XPS test, and the direction of the electron transfer is from  $\text{BiVO}_4$  to  $\text{NiCo}_2\text{O}_3$ .

Photoluminescence (PL) spectroscopy was conducted on pure  $\text{BiVO}_4$ , pure  $\text{NiCo}_2\text{O}_3$ , and  $\text{BiVO}_4@/\text{NiCo}_2\text{O}_3$  samples to characterize their photo-generated electron-hole separation efficiency. As shown in Figure 9a, the PL spectra revealed that for  $\text{BiVO}_4@/\text{NiCo}_2\text{O}_3-0.67$  and  $\text{BiVO}_4@/\text{NiCo}_2\text{O}_3-1$  samples with lower loading amounts of  $\text{NiCo}_2\text{O}_3$ , their PL spectra are similar to  $\text{BiVO}_4$ , with slightly lower PL peak intensities compared to the  $\text{BiVO}_4$  sample. The  $\text{BiVO}_4@/\text{NiCo}_2\text{O}_3-0.67$  sample exhibits the lowest PL peak intensity, indicating the lowest electron-hole recombination rate. Meanwhile, for  $\text{BiVO}_4@/\text{NiCo}_2\text{O}_3-2$  and  $\text{BiVO}_4@/\text{NiCo}_2\text{O}_3-5$  samples with higher  $\text{NiCo}_2\text{O}_3$  contents, their PL spectra show more characteristics of  $\text{NiCo}_2\text{O}_3$ , and their PL peak intensities are significantly lower than those of pure  $\text{NiCo}_2\text{O}_3$  samples. These results suggest that the construction of heterojunctions can effectively promote photocarrier generation and separation for both  $\text{BiVO}_4$  and  $\text{NiCo}_2\text{O}_3$ .

In order to more intuitively understand the influence of  $\text{NiCo}_2\text{O}_3$  loading ratio on the ability of catalyst to generate  $\cdot\text{OH}$  under light, coumarin fluorescence method was used to detect the  $\cdot\text{OH}$  production of different samples. In this study, the fluorescence intensity of the samples correlates directly with

the  $\cdot\text{OH}$  level. Figure 9b illustrates the fluorescence intensities of pure  $\text{BiVO}_4$  and heterojunction samples. Pure  $\text{BiVO}_4$  exhibits relatively low fluorescence intensity, indicating its limited ability to generate  $\cdot\text{OH}$ . Among the heterojunction samples, the  $\text{BiVO}_4@/\text{NiCo}_2\text{O}_3-2$  sample demonstrates the highest fluorescence intensity, followed by the  $\text{BiVO}_4@/\text{NiCo}_2\text{O}_3-5$  sample. Upon analysis of the experimental data, it is evident that as the  $\text{NiCo}_2\text{O}_3$  loading ratio gradually increases, the  $\cdot\text{OH}$  generation by the heterojunction catalyst initially rises and then declines. This result aligns with the variation in photocatalytic performance with  $\text{NiCo}_2\text{O}_3$  loading ratio. Moreover, considering the trend in photocurrent response, it can be inferred that an appropriate amount of  $\text{NiCo}_2\text{O}_3$  loading enhances the charge separation efficiency of the catalyst, increases the  $\cdot\text{OH}$  production, and thereby promotes  $\text{CO}_2$  reduction.

EPR spectra were obtained to identify the generated free radicals during the reaction process and elucidate the charge transfer pathways between  $\text{BiVO}_4$  and  $\text{NiCo}_2\text{O}_3$ . Since the CB potential of  $\text{BiVO}_4$  is more positive than the standard potential of  $\text{O}_2/\cdot\text{O}_2^-$  (0.084 V vs. RHE), it can be concluded that  $\cdot\text{O}_2^-$  cannot be generated on  $\text{BiVO}_4$ . As shown in Figures 10a, no signals were detected for both  $\text{BiVO}_4$  and  $\text{BiVO}_4@/\text{NiCo}_2\text{O}_3-2$  samples under dark conditions,  $\text{BiVO}_4$  exhibited observable EPR signals of  $\text{DMPO}\cdot\text{OH}$  adducts with an intensity ratio of 1:2:2:1 under visible light irradiation. For the  $\text{BiVO}_4@/\text{NiCo}_2\text{O}_3-2$  sample, a more pronounced EPR signal was observed, indicating there are more photogenerated holes on  $\text{BiVO}_4$  to produce  $\cdot\text{OH}$ . Additionally, as shown in Figure 10b, EPR signals of  $\text{DMPO}\cdot\text{O}_2^-$  adducts were detected on  $\text{NiCo}_2\text{O}_3$ . The EPR signal intensity of the  $\text{BiVO}_4@/\text{NiCo}_2\text{O}_3-2$  sample did not significantly increase, but the peak exhibited changes in peak shape. This may be attributed to the overlapping of peaks caused by certain intermediates. The results from EPR analysis suggest that compared to the homogeneous structure of the pure samples, the heterojunction  $\text{BiVO}_4@/\text{NiCo}_2\text{O}_3-2$  sample exhibits enhanced generation of  $\cdot\text{OH}$  and  $\cdot\text{O}_2^-$  under illumination. This result further illustrates how the heterojunction construction facilitates charge transfer between  $\text{BiVO}_4$  and  $\text{NiCo}_2\text{O}_3$ , thereby facilitating the  $\text{CO}_2$  reduction process.

Based on the above results, the reaction path of photo-reduction of  $\text{CO}_2$  to  $\text{CO}$  by heterojunction catalyst was speculated:

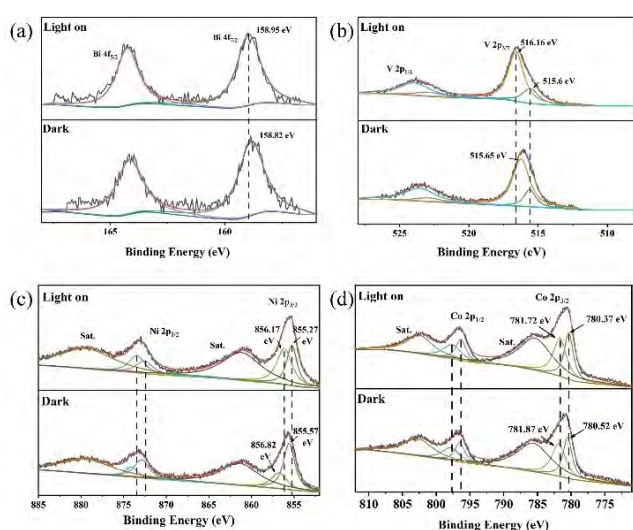


**Figure 8.** In-situ XPS spectra of (a) Bi 4f, (b) V 2p, (c) Ni 2p and (d) Co 2p of  $\text{BiVO}_4@/\text{NiCo}_2\text{O}_3-2$ .

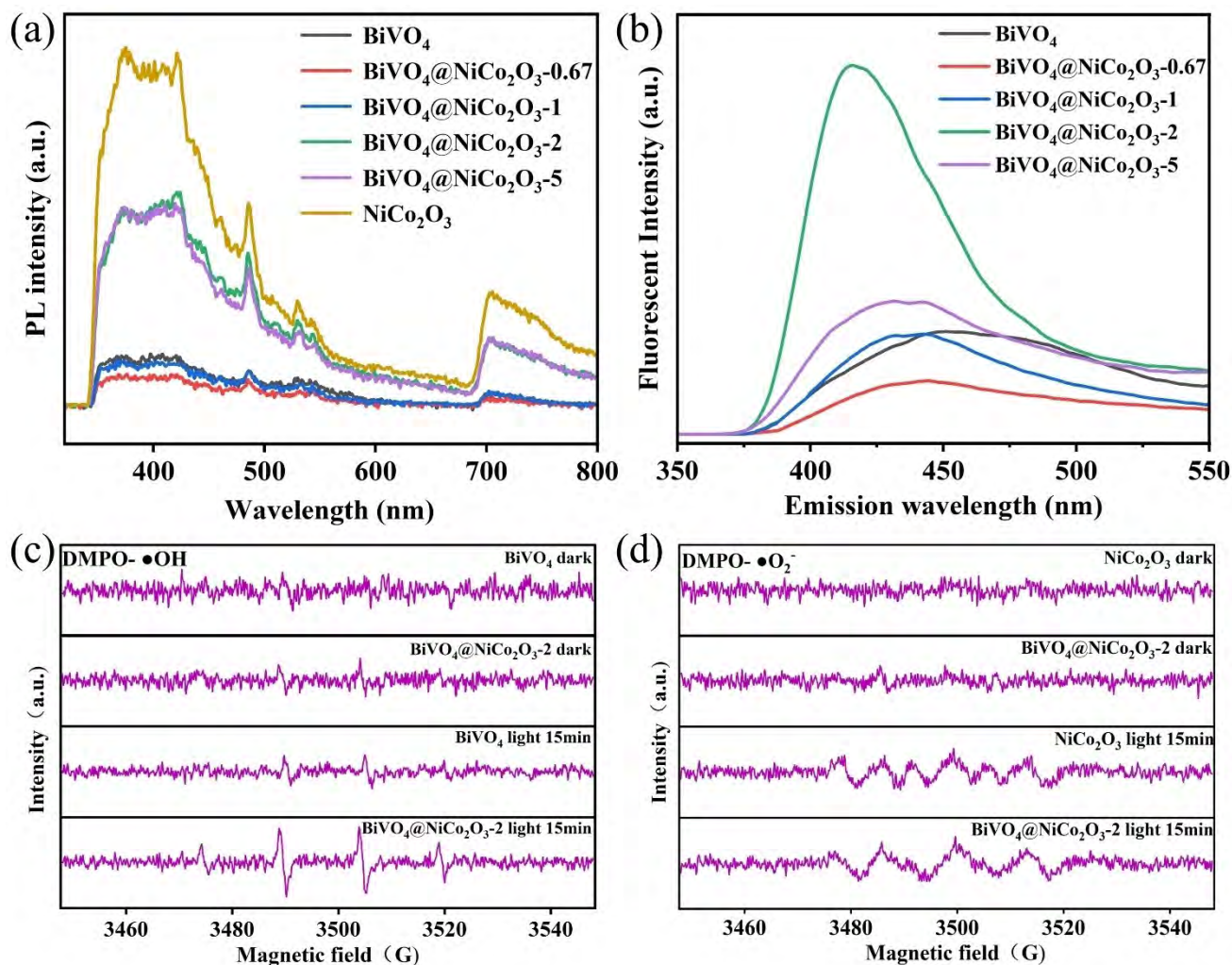


**Figure 9.** (a) Photoluminescence spectroscopy of BiVO<sub>4</sub>, NiCo<sub>2</sub>O<sub>3</sub> and BiVO<sub>4</sub>@NiCo<sub>2</sub>O<sub>3</sub> samples. (b) Fluorescent spectra related to the formed hydroxyl radical amount of BiVO<sub>4</sub> and BiVO<sub>4</sub>@NiCo<sub>2</sub>O<sub>3</sub> samples. DMPO spin-trapping EPR spectra for •OH (c) and •O<sub>2</sub><sup>-</sup> (d) under visible-light irradiation for BiVO<sub>4</sub>, NiCo<sub>2</sub>O<sub>3</sub> and BiVO<sub>4</sub>@NiCo<sub>2</sub>O<sub>3</sub>-2 heterojunction.

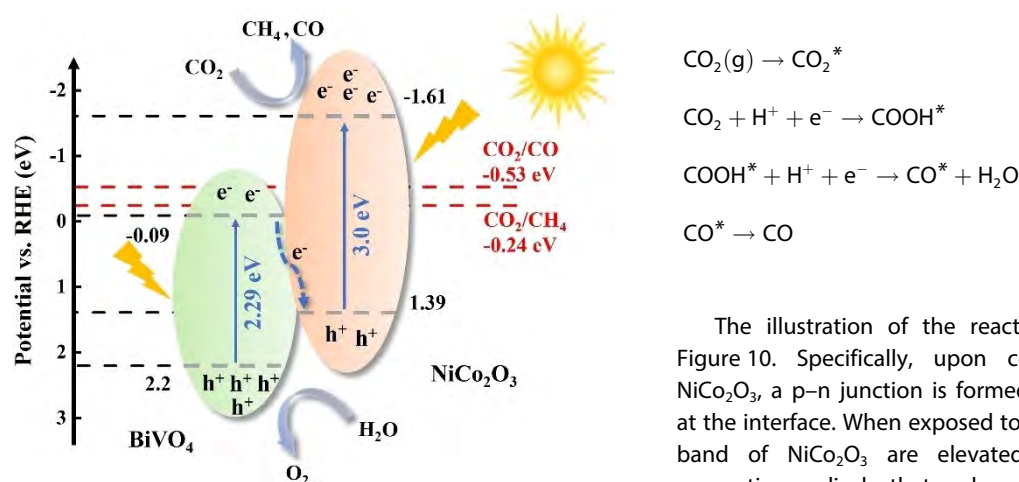
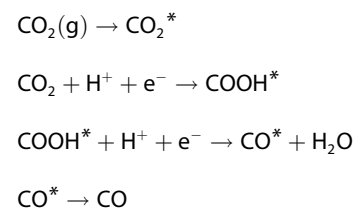


**Figure 10.** Illustration of the reaction mechanism for photocatalytic CO<sub>2</sub> reduction over the BiVO<sub>4</sub>@NiCo<sub>2</sub>O<sub>3</sub> heterojunction under irradiation.



The illustration of the reaction mechanism is shown in Figure 10. Specifically, upon contact between BiVO<sub>4</sub> and NiCo<sub>2</sub>O<sub>3</sub>, a p-n junction is formed, leading to electron transfer at the interface. When exposed to light, electrons in the valence band of NiCo<sub>2</sub>O<sub>3</sub> are elevated to the conduction band, generating radicals that reduce CO<sub>2</sub> molecules adsorbed on metal sites. Simultaneously, electrons from the conduction band of BiVO<sub>4</sub> shift to the valence band of NiCo<sub>2</sub>O<sub>3</sub> through the heterogeneous interface and recombine with the photogenerated holes.

## Conclusions

In summary, a heterojunction of BiVO<sub>4</sub>@NiCo<sub>2</sub>O<sub>3</sub> exhibiting substantial photocatalytic activity for CO<sub>2</sub> conversion has been successfully synthesized. In a liquid-solid reaction system without sacrificial agents, the optimized catalyst exhibited a significantly improved CO production rate of 7.202 μmol·g<sup>-1</sup>·h<sup>-1</sup> compared to that of pure NiCo<sub>2</sub>O<sub>3</sub> (4.726 μmol·g<sup>-1</sup>·h<sup>-1</sup>). XPS spectroscopy and other analyses indicate that this enhancement can be attributed to charge transfer and separation at the hetero-interface. Upon light excitation, electrons shift from BiVO<sub>4</sub> to NiCo<sub>2</sub>O<sub>3</sub>, facilitating CO<sub>2</sub> reduction on the NiCo<sub>2</sub>O<sub>3</sub>, thereby enhancing the CO generation rate. This study provides a feasible approach for constructing photocatalysts for CO<sub>2</sub> reduction in aqueous environments.

## Acknowledgements

This work was financially supported by the National Natural Science Foundation of China (52072387), the Key Collaborative Research Program of the Alliance of International Science Organization (ANSO-CR-KP-2020-13), the Natural Science Foundation of Shanghai (22ZR1471800).

## Conflict of Interests

The authors declare no conflict of interest.

## Data Availability Statement

The data that support the findings of this study are available from the corresponding author upon reasonable request.

**Keywords:** Carbon dioxide photoreduction · Bismuth vanadate · Rock-salt oxides · heterojunction

- [1] a) D. Shindell, C. J. Smith, *Nature* **2019**, *573*, 408–411; b) T. A. Saleh, *RSC Adv.* **2022**, *12*, 23869–23888; c) W. Tu, Y. Zhou, Z. Zou, *Adv. Mater.* **2014**, *26*, 4607–4626; d) L. Wang, W. Chen, D. Zhang, Y. Du, R. Amal, S. Qiao, J. Wu, Z. Yin, *Chem. Soc. Rev.* **2019**, *48*, 5310–5349.  
[2] J. Gu, W. Chen, G. G. Shan, G. Li, C. Sun, X. L. Wang, Z. Su, *Mater. Today Energy* **2021**, *21*, 17.  
[3] a) H. B. Huang, H. Y. Zhang, F. Y. Cai, Y. F. Li, J. Lü, R. Cao, *J. Mater. Chem. A* **2021**, *9*, 20350–20355; b) Z. Z. Yu, K. Yang, C. L. Yu, K. Q. Lu, W. Y.

Huang, L. Xu, L. X. Zou, S. B. Wang, Z. Chen, J. Hu, Y. Hou, Y. F. Zhu, *Adv. Funct. Mater.* **2022**, *32*, 10.

- [4] a) Y. Chai, L. Li, J. N. Shen, Y. F. Zhang, J. Liang, *ACS Appl. Energ. Mater.* **2022**, *5*, 3748–3756; b) Y. Liu, P. F. Tan, L. Yang, H. W. Liu, J. Pan, *J. Mater. Sci. Mater. Electron.* **2023**, *34*, 13.  
[5] a) X. Y. Li, M. Wang, R. Y. Wang, M. Shen, P. Wu, Z. Q. Fu, M. Zhu, L. X. Zhang, *J. Colloid Interface Sci.* **2022**, *615*, 821–830; b) X. Shi, L. Wang, W. D. Dai, X. A. Dong, Y. Bai, L. Q. Ye, *ACS Catal.* **2023**, *13*, 5264–5271.  
[6] a) Y. Q. He, Q. Lei, C. G. Li, Y. Han, Z. Shi, S. H. Feng, *Mater. Today* **2021**, *50*, 358–384; b) R. R. Pan, J. Liu, J. T. Zhang, *ChemNanoMat* **2021**, *7*, 737–747.  
[7] Z. P. Wang, Z. P. Lin, S. J. Shen, W. W. Zhong, S. W. Cao, *Chin. J. Catal.* **2021**, *42*, 710–730.  
[8] M. Tahir, B. Tahir, *J. Mater. Sci. Technol.* **2022**, *106*, 195–210.  
[9] Z. Z. Zhang, X. H. Liu, Y. L. Li, H. Yu, W. J. Li, H. B. Yu, *Appl. Catal. B* **2022**, *319*, 12.  
[10] Y. Li, Y.-L. Yang, G. Chen, J.-J. Fan, Q.-J. Xiang, *Rare Met.* **2022**, *41*, 3045–3059.  
[11] a) Q. Zhang, P. J. Yang, H. X. Zhang, J. H. Zhao, H. Shi, Y. M. Huang, H. Q. Yang, *Appl. Catal. B* **2022**, *300*, 12; b) S. Roy, E. Reisner, *Angew. Chem. Int. Ed.* **2019**, *58*, 12180–12184.  
[12] a) X. Sun, J. Sun, C. Wu, L. Guo, L. Hou, C. Yuan, *Mater. Today Energy* **2021**, *19*, 8; b) Y. Zhang, X. X. Wang, F. Q. Luo, Y. Tan, L. X. Zeng, B. Z. Fang, A. H. Liu, *Appl. Catal. B* **2019**, *256*, 10; c) K. Fominykh, G. C. Tok, P. Zeller, H. Hajiyani, T. Miller, M. Döblinger, R. Pentcheva, T. Bein, D. Fattakhova-Rohlfing, *Adv. Funct. Mater.* **2017**, *27*, 1605121.  
[13] L. Li, X. Dai, D.-L. Chen, Y. X. Zeng, Y. Hu, X.-W. Lou, *Angew. Chem. Int. Ed.* **2022**, *61*, e202205839.  
[14] a) S. C. Wang, L. Z. Wang, W. Huang, *J. Mater. Chem. A* **2020**, *8*, 24307–24352; b) L. Q. Ye, Y. Deng, L. Wang, H. Q. Xie, F. Y. Su, *ChemSusChem* **2019**, *12*, 3671–3701.  
[15] a) S. J. Song, Z. P. Xing, H. A. Zhao, Z. Z. Li, W. Zhou, *Green Energy & Environ.* **2023**, *8*, 1232–1264; b) Z. L. Zhao, J. Bian, L. Zhao, H. J. Wu, S. Xu, L. Sun, Z. J. Li, Z. Q. Zhang, L. Q. Jing, *Chin. J. Catal.* **2022**, *43*, 1331–1340.  
[16] X. Wei, J. Zhang, L. Wang, Y. Bai, J. Huang, H. She, Q. Wang, *Chem. Eng. J.* **2024**, *482*, 149114.  
[17] D. Philo, S. Q. Luo, C. He, Q. Wang, F. Ichihara, L. L. Jia, M. Oshikiri, H. Pang, Y. Wang, S. J. Li, G. L. Yang, X. H. Ren, H. W. Lin, J. H. Ye, *Adv. Funct. Mater.* **2022**, *32*, 10.  
[18] J. Zhang, X. Wei, J. Zhao, Y. Zhang, L. Wang, J. Huang, H. She, Q. Wang, *Chem. Eng. J.* **2023**, *454*, 140081.  
[19] N. Alidoust, M. Lessio, E. A. Carter, *J. Appl. Phys.* **2016**, *119*, 9.  
[20] S. Wang, B. Y. Guan, X. W. Lou, *Energy & Environmental Science* **2018**, *11*, 306–310.  
[21] W.-W. Dong, J. Jia, Y. Wang, J.-R. An, O.-Y. Yang, X.-J. Gao, Y.-L. Liu, J. Zhao, D.-S. Li, *Chem. Eng. J.* **2022**, *438*, 135622.  
[22] F. G.-R. Luis, M. T.-M. Leticia, L. Elisa, M. Edgar, *J. Energy Chem.* **2019**, *37*, 18–28.  
[23] L. Huang, D. Hou, S. Gan, X. Q. Qiao, D. S. Li, *ChemCatChem* **2021**, *13*, 3357–3367.  
[24] C. Kim, K. M. Cho, A. Al-Saggaf, I. Gereige, H.-T. Jung, *ACS Catal.* **2018**, *8*, 4170–4177.  
[25] X.-M. Cheng, X.-Y. Dao, S.-Q. Wang, J. Zhao, W.-Y. Sun, *ACS Catal.* **2021**, *11*, 650–658.

Manuscript received: April 27, 2024  
Revised manuscript received: June 4, 2024  
Accepted manuscript online: June 26, 2024  
Version of record online: August 30, 2024